Nanoscale Advances

ROYAL SOCIETY OF CHEMISTRY

PAPER

View Article Online
View Journal | View Issue

Cite this: *Nanoscale Adv.*, 2024, **6**, 2363

Revealing the synergistic effect of Ni single atoms and adjacent 3d metal doped Ni nanoparticles in electrocatalytic CO_2 reduction†

Yingjie Liu,‡[a] Zhaohui Wu,‡[a] Sha Bai,[a] Tianyang Shen,[a] Qian Li,[a] Guihao Liu,[a] Xiaoliang Sun,[a] Yihang Hu,[a] Ziheng Song,[a] Jinfeng Chu*[a] and Yu-Fei Song *[ab]

Herein, we report the successful fabrication of a series of transition metal doped Ni nanoparticles (NPs) coordinated with Ni single atoms in nitrogen-doped carbon nanotubes (denoted as Ni_{1+NPs}M-NCNTs, M = Mn, Fe, Co, Cu and Zn; Ni_1 = Ni single atom). X-ray absorption fine structure reveals the coexistence of Ni single atoms with Ni–N_4 coordination and NiM NPs. When applied for electrocatalytic CO_2RR, the Ni_{1+NPs}M-NCNT compounds show the Faradaic efficiency of CO (FE_{CO}) with a volcano-like tendency of Mn < Fe ≈ Co < Zn < Cu, in which the Ni_{1+NPs}Cu-NCNT exhibits the highest FE_{CO} of 96.92%, a current density of 171.25 mA cm^{-2} and a sustainable stability over 24 hours at a current density of 100 mA cm^{-2}, outperforming most reported examples in the literature. Detailed experiments and theoretical calculations reveal that for Ni_{1+NPs}Cu-NCNTs, the electron transfer from NiCu NPs to Ni single atoms strengthens the adsorption of *COOH intermediates. Moreover, the d-band center of Ni–N in Ni_{1+NPs}Cu-NCNT is upshifted, providing stronger binding with the reaction intermediates of *COOH, whereas the NiCu NPs increase the Gibbs free energy change of the Volmer step, suppressing the competitive HER.

Received 28th February 2024
Accepted 15th March 2024

DOI: 10.1039/d4na00167b

rsc.li/nanoscale-advances

Introduction

Due to the burning of fossil fuels and human activities, excessive emission of CO_2 has increased in the past decades, which quickens the pace of global warming and the rise of sea level.[1–4] Electrochemical CO_2RR is an efficient method to make use of the greenhouse gas CO_2 for its clean energy source and operational convenience.[5–7] Among multiple products in the CO_2RR, the two-electron product CO stands out as one of the most economically favorable products per unit of electrical energy input in the CO_2 reduction reaction (CO_2RR). It also serves as a crucial industrial feedstock in Fischer–Tropsch synthesis for producing multi-carbon chemicals. Despite its importance, the CO_2RR to CO faces several challenges, including the activation of CO_2 and slow hydrogenation kinetics, resulting in a high energy barrier for the overall electrocatalytic reaction. In addition, the overpotential of the CO_2RR is higher than that of the competing hydrogen evolution reaction (HER), which makes the selectivity of the CO_2RR hard to control.[8–12] Therefore, it's of vital importance to fabricate an efficient catalyst to promote CO_2RR to CO.

Single atom catalysts (SACs) with high utilization of atoms have emerged as a variety of promising materials in the CO_2RR and their distinct active sites are ascertained to be effective sites to produce CO.[13–15] In recent years, SACs containing Mn,[16] Fe,[17–19] Co,[20,21] Ni,[22,23] Cu[24] and Zn[25,26] have been widely applied for the CO_2RR and been demonstrated as outstanding catalysts with high selectivity. However, during the CO_2RR, CO_2 and H_2O need to be simultaneously activated. SACs with uniform single designated active sites may not offer the optimized performance, which calls for new strategies for catalyst design.[27,28] Metal nanoparticles, such as Ni and Fe, are capable of promoting H_2O splitting, which can accelerate proton-feeding to generate the key intermediate *COOH.[29,30] Recently, Ren *et al.* reported that the high conductivity of Ni NPs can modulate the electronic structure of single sites, which would further promote the adsorption of *COOH intermediates.[31] However, excessive Ni NPs would promote the HER, resulting in much more H_2 production and low CO selectivity. Hence, it's of great importance to promote the CO_2 activation and to restrain the side HER by rational design of catalysts in order to guarantee the kinetic balance and performance of CO_2RR to CO.[32,33]

Herein, we report the pyrolysis of the mixture of NiMAl-LDH (M = Mn, Fe, Co, Cu and Zn) and melamine, which results in the formation of the co-existence of 3d transition metal doped Ni NPs and Ni single atoms that are encapsulated by N-doped carbon nanotubes (denoted as Ni_{1+NPs}M@NCNT, M = Mn, Fe,

[a]*State Key Laboratory of Chemical Resource Engineering, Beijing University of Chemical Technology, Beijing 100029, P. R. China. E-mail: jfchu@163.com; songyf@mail.buct.edu.cn; Fax: +86 10 64431832; Tel: +86 10 64431832*

[b]*Quzhou Institute for Innovation in Resource Chemical Engineering, Quzhou 324000, Zhejiang Province, P. R. China*

† Electronic supplementary information (ESI) available. See DOI: https://doi.org/10.1039/d4na00167b

‡ These authors contributed equally to this work.

Co, Cu and Zn). The electron density on Ni single atoms in $Ni_{1+NPs}M$@NCNT can be successfully regulated by introducing 3d transition metals in Ni NPs. The $Ni_{1+NPs}Cu$@NCNT exhibits the best FE_{CO} of 92.06% and a satisfying stability over 24 h. Moreover, when applied in a flow cell, the $Ni_{1+NPs}Cu$@NCNT achieves a current density of 200 mA cm^{-2} and a FE_{CO} above 90% over a wide range of 0.38 V to −1.08 V (*vs.* RHE). The DFT calculation proves that the NiM NPs can not only promote electron transfer to the active single Ni sites, but also upshift the 3d orbital of Ni, thus improving the intrinsic activity of Ni atoms.

Results and discussion

Synthesis and characterization

The $Ni_{1+NPs}M$@NCNT compounds are synthesized according to the literature with slight modification.[33] Typically, NiMAl-LDHs (M = Mn, Fe, Co, Cu, Zn) are synthesized by the coprecipitation method, whose X-ray diffraction (XRD) patterns show characteristic diffraction peaks corresponding to (00l) facets that match well with LDHs (Fig. S1†). Melamine is chosen as the source of carbon and nitrogen and then mixed with NiMAl-LDHs for the following calcination at 650 °C.[31] Acid-leaching is applied to remove the acid soluble impurities of Ni_{1+NPs}-M@NCNTs. The XRD pattern (Fig. S2†) shows diffraction peaks corresponding to (002) of graphite and (111) and (200) of Ni metal, which preliminarily prove the existence of Ni NPs and that structural modification caused by M doping is negligible. As presented in Fig. S3,† Raman spectra display a D band at about 1350 cm^{-1} and a G band at 1600 cm^{-1}, which can be attributed to amorphous and ordered sp^2 carbon, respectively.[32,34] Intensity ratios between the two bands (I_D/I_G) can measure the defect degree of carbon-based materials. I_D/I_G

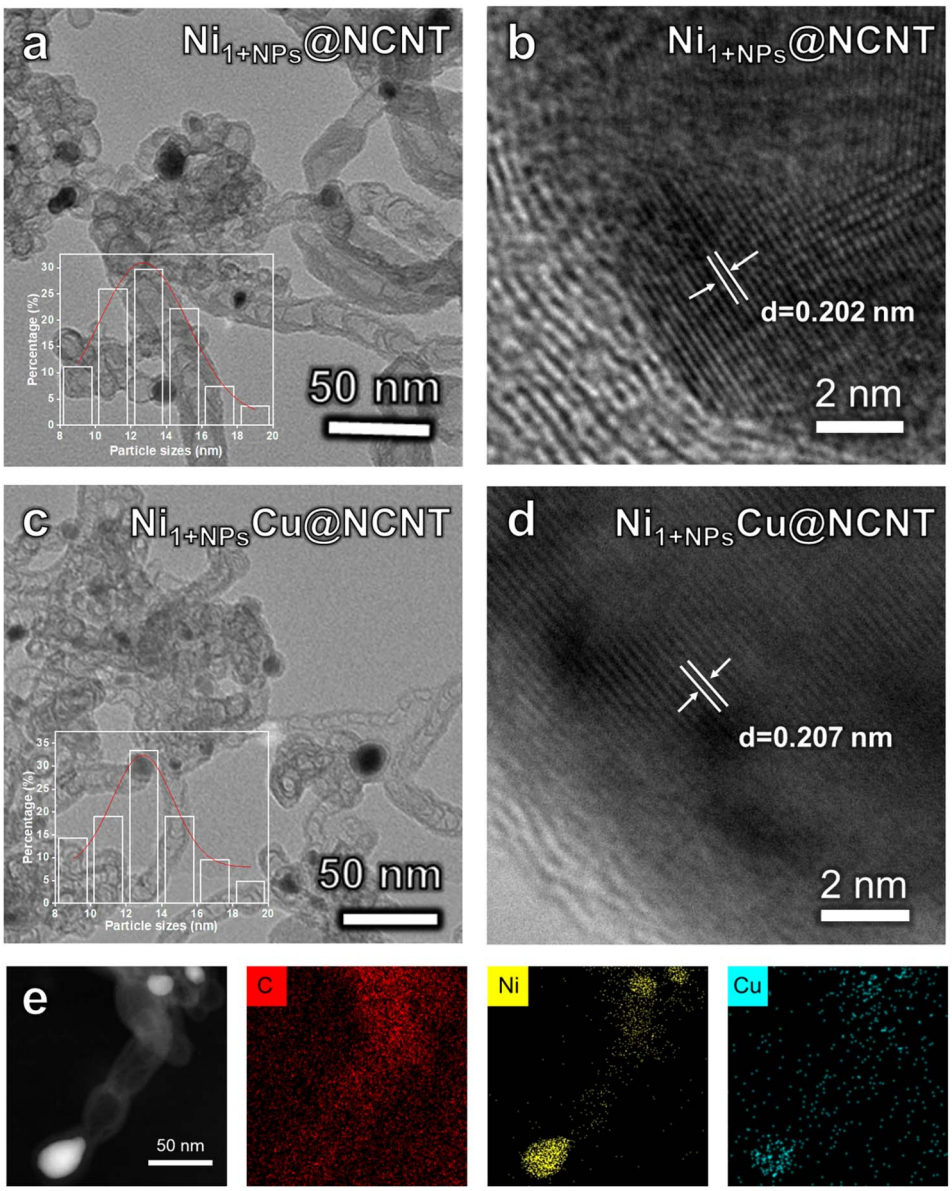

Fig. 1 TEM and High-resolution transmission electron microscopy (HRTEM) images of (a and b) Ni_{1+NPs}@NCNT and (c and d) $Ni_{1+NPs}Cu$@NCNT; (e) EDX elemental mapping images of the $Ni_{1+NPs}Cu$@NCNT.

values of $Ni_{1+NPs}M$@NCNT compounds are similar, indicating their unaffected graphitization degree. As shown in Fig. S4,† scanning electron microscopy (SEM) proves that Ni_{1+NPs}-M@NCNT compounds are composed of carbon nanotubes. In addition, transmission electron microscopy (TEM) and high-resolution transmission electron microscopy (HR-TEM) present NPs encapsulated in the carbon shell. As a result, the diameter of carbon nanotubes and the size of trapped NPs are measured to range from 10 nm to 20 nm (Fig. 1a, c and S5†). As shown in Fig. 1d, the lattice fringes of the NPs in Ni_{1+NPs}-Cu@NCNT are calculated to be 0.207 nm, which is slightly larger than that of pure Ni NPs (0.202 nm, Fig. 1b), matching well with NiCu.[35] Moreover, energy dispersive X-ray spectroscopy (EDX) elemental mapping images (Fig. 1e and S6†) reveal that C and N are uniformly distributed in the catalyst. Ni signals not only aggregate in the NPs, but also uniformly distribute throughout the carbon nanotube, demonstrating the uniform distribution of Ni single atoms. On the other hand, Cu can only be detected in the NP. In addition, the EDX line scan results in Fig. S7† reveal that both Cu and Ni can be detected in the NP but no Cu signal can be detected in NCNTs. These results preliminarily prove the basically non-existing Cu single sites compared to Ni single atoms and successfully synthesized NiCu NPs.

X-ray absorption fine structure (XAFS) analysis is conducted to examine the electronic structures and chemical configurations of the metal elements. Ni K-edge X-ray absorption near-edge spectroscopy (XANES) spectra are displayed in Fig. 2a; the absorption edges of $Ni_{1+NPs}Cu$@NCNT and Ni_{1+NPs}@NCNT are located nearly the same as that of Ni-foil, which proves that metallic Ni is the dominating species in NCNTs. Nevertheless, the oscillations of $Ni_{1+NPs}Cu$@NCNT and Ni_{1+NPs}@NCNT in the E space are different from that of Ni-foil, suggesting that the coordination environments are not exactly alike. The extended XAFS (EXAFS) were Fourier transformed (FT) k^3-weighted to further detect the fine structure of the samples (Fig. 2b). For $Ni_{1+NPs}Cu$@NCNT and Ni_{1+NPs}@NCNT, both coordination shells of Ni–N (1.49 Å) and Ni–Ni (2.04 Å) can be observed, Furthermore, the coordination number (CN) of Ni–N is obtained from the EXFAS fitting results and the average values in $Ni_{1+NPs}Cu$@NCNT and Ni_{1+NPs}@NCNT are determined to be 3.91 and 3.96, respectively (Fig. 2c and d). The EXAFS fitting results show that the first shell can be attributed to the $Ni–N_4$ coordination, which is in good agreement with the reported literature.[22,35] The EXAFS results demonstrate the co-existence of Ni NPs and single atoms, which is in good line with the TEM results. On the other hand, in Cu K-edge XANES, the pre-edge of $Ni_{1+NPs}Cu$@NCNT performs basically the same as that of Cu foil (Fig. S9†), indicating that Cu mainly exist as metallic species. Such results agree well with EDX mapping results to affirm that Cu mainly exists in the NPs rather than single sites coordinated with N.

X-ray photoelectron spectroscopy (XPS) is then applied to investigate the elementary composition of $Ni_{1+NPs}M$@NCNT. As shown in Fig. S11a,† the N 1s spectra of Ni_{1+NPs}@NCNT and $Ni_{1+NPs}M$@NCNT (M = Mn, Fe, Cu) are located at similar binding energy and display identical shape features, which can be deconvoluted into five species: pyridinic N (398.9 eV), Ni–N (400.3 eV), pyrrolic N (400.4 eV), graphitic N (401.6 eV) and oxidized N (403.3 eV).[36] Meanwhile, the quantitative integral reveals that the contents of the N species are also similar in the four samples. In Fig. S11b† and 2e, the Ni $2p^{2/3}$ spectra can be split into two peaks assigned to $Ni^{\delta+}$ ($0< \delta < 2$) and metallic Ni^0, respectively. Notably, the $Ni^{\delta+}$ peak shifts as follows: Ni_{1+NPs}@NCNT (855.06 eV) > $Ni_{1+NPs}Mn$@NCNT (855.03 eV) > $Ni_{1+NPs}Fe$@NCNT (854.94 eV) > $Ni_{1+NPs}Cu$@NCNT (854.75 eV). These demonstrate that electrons are transferred from NiM NPs

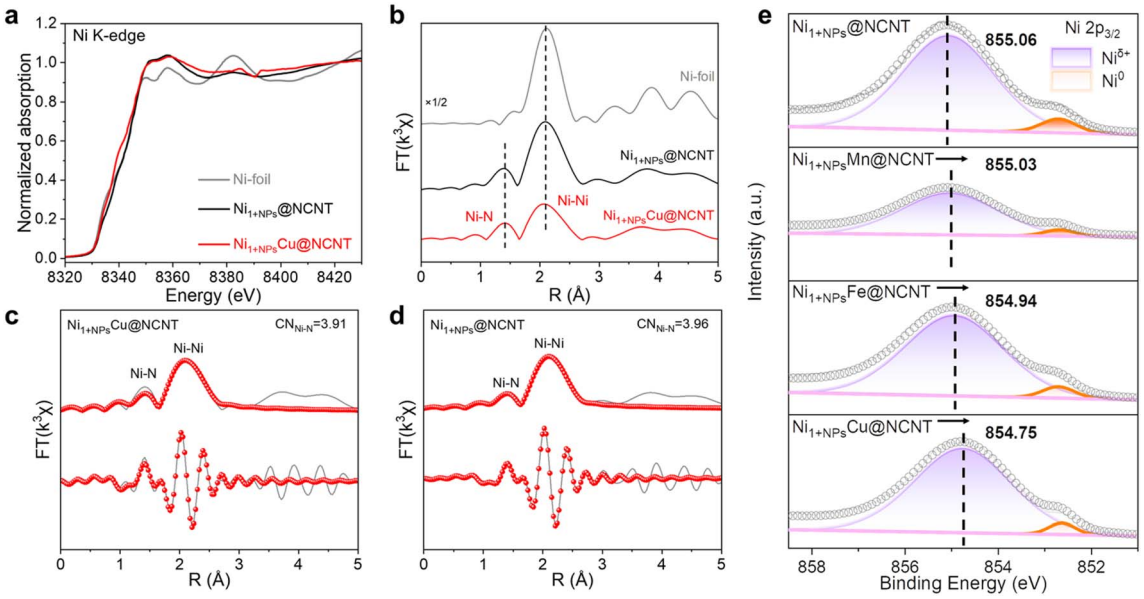

Fig. 2 (a) Ni K-edge XANES spectra and (b) Fourier transform EXAFS spectra in the R space of $Ni_{1+NPs}Cu$@NCNT, Ni_{1+NPs}@NCNT and Ni foil; EXAFS fitting results of (c) Ni_{1+NPs}@NCNT; and (d) $Ni_{1+NPs}Cu$@NCNT; (e) enlarged Ni 2p XPS spectra of Ni_{1+NPs}@NCNT, $Ni_{1+NPs}Mn$@NCNT, $Ni_{1+NPs}Fe$@NCNT and $Ni_{1+NPs}Cu$@NCNT.

to the $Ni^{\delta+}$ atoms and result in electron accumulation on the Ni–N_4 sites.

CO_2RR performance

The as-prepared $Ni_{1+NPs}M$@NCNT catalysts are then applied to electrochemical CO_2RR to evaluate their catalytic performance, which is first operated in an H-type cell. The linear sweep voltammetry (LSV) curves taken in 0.25 M $KHCO_3$ saturated with Ar or CO_2 are compared in Fig. S12;† all six samples show great enhancement in current density when CO_2 is injected into the electrolyte, indicating that the catalysts possess great capability for CO_2 reduction. FE_{CO} values of all catalysts under potentials ranging from −0.59 to −1.19 V (*vs.* RHE) are then measured and presented in Fig. S14a† and 3a. The gas chromatography (GC) and ^1H nuclear magnetic resonance (NMR) analyses are applied to detect the gaseous and liquid products, respectively (Fig. S13†). No other products except for CO and H_2 can be traced. All the $Ni_{1+NPs}M$@NCNT compounds show a higher FE_{CO} than that of Ni_{1+NPs}@NCNT and display a tendency of Mn < Fe ≈ Co < Zn < Cu. Among them, the $Ni_{1+NPs}Cu$@NCNT outperforms others by a wide margin and reaches the highest FE_{CO} of 92.06% at −0.89 V (*vs.* RHE). The partial current density of CO is then calculated and shown in Fig. S14b† and 3b, where $Ni_{1+NPs}Cu$@NCNT surpasses Ni_{1+NPs}@NCNT (17.5 mA cm^{-2}) with an outstanding value of 21.8 mA cm^{-2} at −0.89 (*vs.* RHE).

To meet the industrial demand for abundant CO production, the CO_2RR of $Ni_{1+NPs}Cu$@NCNT is then tested in a flow cell equipped with gas diffusion electrodes (GDEs). The current density reaches up to 200 mA cm^{-2} at −0.84 V (*vs.* RHE) in 1 M KOH with a CO_2 flow rate of 14 mL min^{-1} (Fig. 3e). Moreover, a high CO selectivity of $Ni_{1+NPs}Cu$@NCNT can also be extended to a wider potential window. As shown in Fig. 3f, a high FE_{CO} of above 90% is achieved under a wide range of applied potentials from −0.38 V to −1.08 V (*vs.* RHE), which reaches the maximum 96.92% at −0.78 V (*vs.* RHE). Such performance exhibits competitive superiority in the CO_2RR when compared with other state-of-the-art catalysts with Ni single atoms (Fig. 3g). The stability of $Ni_{1+NPs}Cu$@NCNT is further tested to prove its practical significance for industrial application (Fig. 3h). After the galvanostatic measurement at 100 mA cm^{-2} for 24 h,

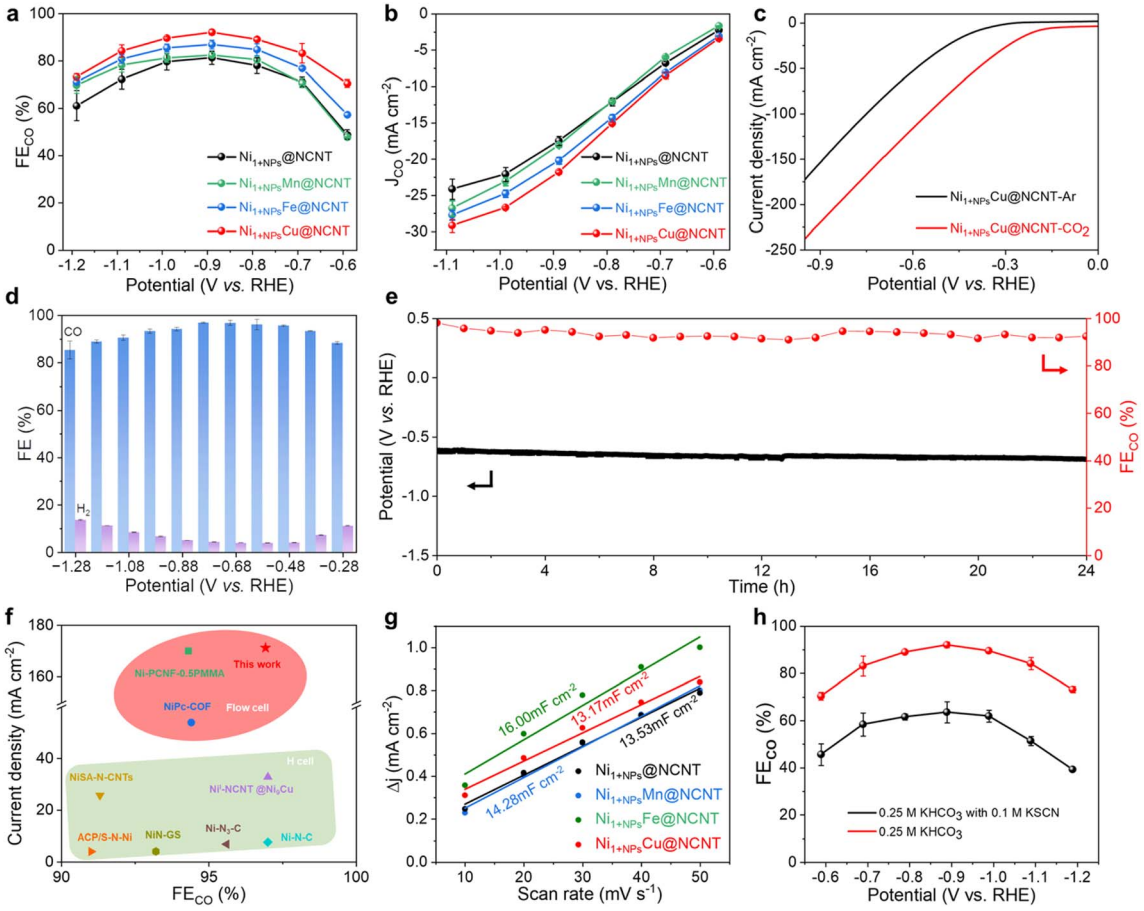

Fig. 3 CO_2RR performance of Ni_{1+NPs}@NCNT, $Ni_{1+NPs}Mn$@NCNT, $Ni_{1+NPs}Fe$@NCNT and $Ni_{1+NPs}Cu$@NCNT. (a) FE_{CO} and (b) J_{CO} of Ni_{1+NPs}@NCNT, $Ni_{1+NPs}Mn$@NCNT, $Ni_{1+NPs}Fe$@NCNT and $Ni_{1+NPs}Cu$@NCNT; CO_2RR performance of $Ni_{1+NPs}Cu$@NCNT in 1 M KOH flow cells. (c) LSV curves under Ar (black) and CO_2 (red) atmospheres; (d) FE_{CO} and FE_{H2} under different potentials; (e) current density and FE_{CO} durability of $Ni_{1+NPs}Cu$@NCNT at 100 mA cm^{-2}; (f) CO_2RR performance of $Ni_{1+NPs}Cu$@NCNT compared to other reported Ni-SACs; (g) the double-layer capacitances of Ni_{1+NPs}@NCNT, $Ni_{1+NPs}Mn$@NCNT, $Ni_{1+NPs}Fe$@NCNT and $Ni_{1+NPs}Cu$@NCNT; (h) FE_{CO} of $Ni_{1+NPs}Cu$@NCNT before and after 0.1 M KSCN treatment.

$Ni_{1+NPs}Cu@NCNT$ maintains a FE_{CO} of above 91% throughout the period and the applied potential only exhibits a slight increase from −0.61 V to −0.69 V (*vs.* RHE). XRD and TEM patterns of $Ni_{1+NPs}Cu@NCNT$ after the reaction display consistent diffraction peaks and morphology (Fig. S16†), illustrating the sustainable durability of $Ni_{1+NPs}Cu@NCNT$.

To elucidate the better CO_2RR performance of Ni_{1+NPs}-Cu@NCNT, electrochemical surface areas (ECSA) of Ni_{1+NPs}-M@NCNT are investigated. ECSAs are obtained from the electrochemical double-layer capacitance (C_{dl}) by measuring cycle curves at scan speeds which increase equally (Fig. S15† and 3c). As a result, approximate values are obtained for $Ni_{1+NPs}@NCNT$, $Ni_{1+NPs}Mn@NCNT$, $Ni_{1+NPs}Fe@NCNT$ and $Ni_{1+NPs}Cu@NCNT$, indicating that the superior performance is more likely to originate from active species rather than the surface area available.[37] Thiocyanate ions (SCN^-) are then added into the electrolyte as an inhibitor to block the metal-N sites, thus illustrating their activity for the CO_2RR.[25] As expected, the FE_{CO} exhibits a significant decline after the addition of SCN^- (Fig. 3d), confirming Ni–N_4 sites to be active centers for the CO_2RR. On the other hand, $Ni_{NPs}@NCNT$ without Ni single atoms is in favor of the HER and the CO production is negligible, explaining that NPs play a role in *H generation for proton feeding.

DFT calculation

To shed light on the enhanced CO-produced CO_2RR performance of $Ni_{1+NPs}Cu@NCNT$, the DFT calculation is further carried out. The free energy profile of the competitive HER is calculated first. All the Gibbs free energy barriers (ΔG_{H^*}) of the Volmer step ($H^+ + e^- \rightarrow H^*$) are increased after 3d transition

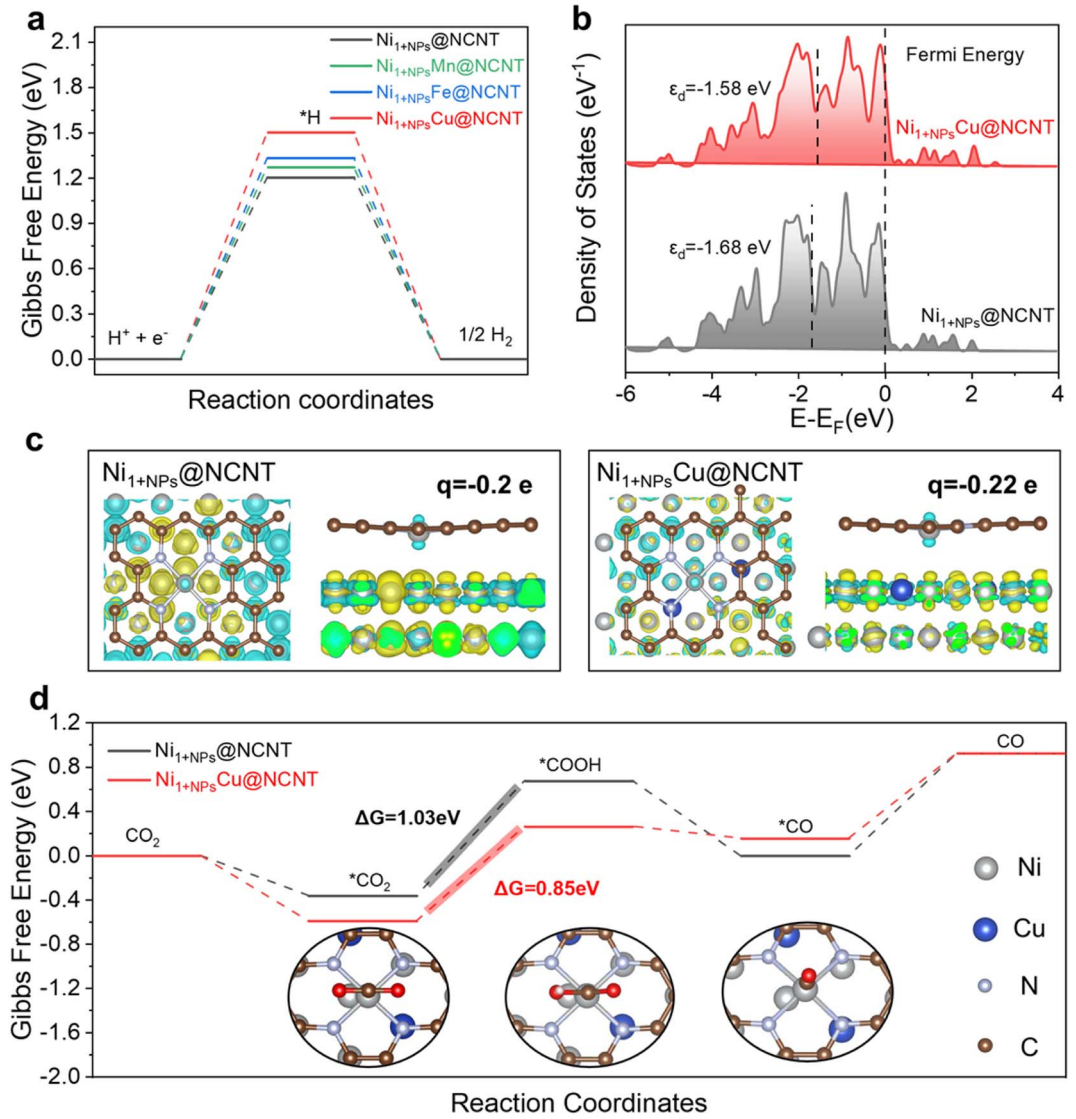

Fig. 4 (a) Calculated Gibbs free energy diagrams of the HER on $Ni_{1+NPs}@NCNT$ and $Ni_{1+NPs}Cu@NCNT$; (b) calculated projected density of states (PDOS) of d orbitals on $Ni_{1+NPs}@NCNT$ and $Ni_{1+NPs}Cu@NCNT$; (c) the plots of electron density difference in $Ni_{1+NPs}@NCNT$ and Ni_{1+NPs}-Cu@NCNT. Blue color indicates the loss of charge and yellow shows the gain of electrons. (d) Calculated Gibbs free energy diagrams of electrocatalytic CO_2RR to CO on $Ni_{1+NPs}@NCNT$ and $Ni_{1+NPs}Cu@NCNT$.

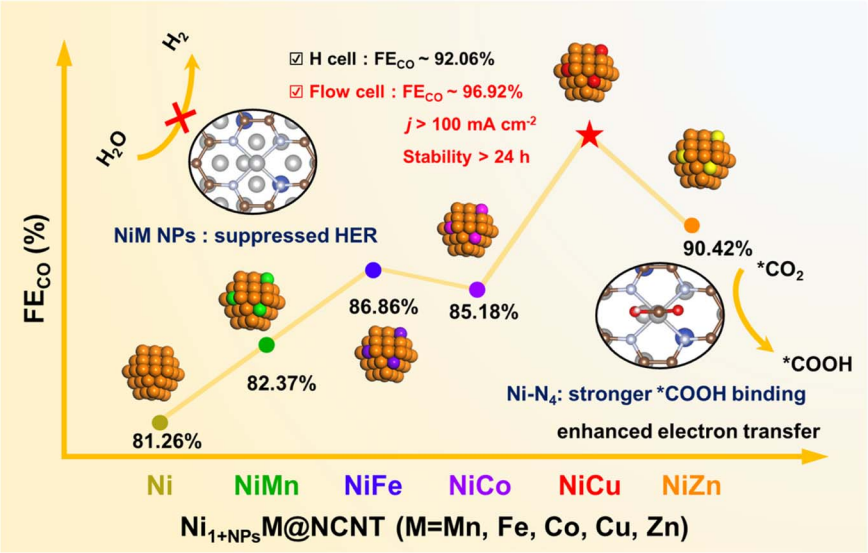

Fig. 5 The schematic illustration of enhanced CO_2RR performance on Ni_{1+NPs}M@NCNTs.

metal doping, revealing the suppression of the HER process. The ΔG_{H^*} increases in the following order: Ni (1.20 eV) < NiMn (1.27 eV) < NiFe (1.33 eV) < NiCu (1.50 eV), which is in good agreement with the sequence of FE_{H2} decrease in Fig. 3, suggesting that ΔG_{H^*} can be an effective indicator for the inhibition of the HER, and thus the Ni_{1+NPs}Cu@NCNT with the highest H* energy barrier among these samples has a most favorable selectivity for CO.

Further electronic structure analysis is employed to understand the Cu doping from an atomistic perspective. The d-band center (ε_d) has been identified as a descriptor of intermediate binding in electrocatalytic systems.[38] The ε_d upshift of Ni 3d orbitals in Ni_{1+NPs}Cu@NCNT (−1.68 eV) compared with Ni_{1+NPs}@NCNT (−1.58 eV) suggests the less occupancy of antibonding states, and thus stronger intermediate binding strength is promisingly obtained. The contour of electron density difference shows that the electron is transferred from Ni SAs to NPs (Fig. 4c). Then Mulliken charge analysis is used for further quantitative analysis.[39,40] It is found that the Mulliken charge of the Ni single site in Ni_{1+NPs}Cu@NCNT (−0.22*e*) is more negative than that in Ni_{1+NPs}@NCNT (−0.2*e*), demonstrating more electrons are accumulated on Ni–N_4 in Ni_{1+NPs}Cu@NCNT, which is consistent with the XPS data. Electron accumulation can also enhance the binding of the reaction site to form the key intermediates. The stronger affinity of the substrate and intermediate will be helpful for the sufficient utilization of active sites and reaction kinetics. Thus, the Gibbs free energy profile of the overall CO_2-to-CO reduction process is calculated to understand the function of Cu doping for the overall pathway. The Ni_{1+NPs}Cu@NCNT shows a lower ΔG for the first CO_2 activation step, indicating CO_2 activation. For the formation step of key intermediate COOH* ($CO_2^* + H^+ + e^- \rightarrow$ COOH*), the free energy barrier decreases to 0.85 eV after Cu doping, which is obviously less than that of pristine Ni_{1+NPs}@NCNT (1.03 eV), suggesting a more thermodynamically favorable CO production. For the CO desorption process, the CO can be desorbed from the surface of Ni_{1+NPs}Cu@NCNT with a lower energy barrier (0.77 eV) compared with Ni_{1+NPs}@NCNT (0.93 eV), which is in line with the optimal FE_{CO} and efficient CO production (Fig. 5).

Conclusion

In summary, we make use of one-step pyrolysis to successfully fabricate a series of Ni_{1+NPs}M (M = Mn, Fe, Co, Cu, Zn) NPs and Ni single atoms that are encapsulated in NCNTs. The HRTEM images confirm the existence of NiM NPs with a size of 10–20 nm. EXAFS further demonstrates the fine structure of the as-prepared Ni_{1+NPs}@NCNTs: Ni single atoms are coordinated to N atoms with a similar Ni–N_4 structure. XPS proves the lower valence of Ni in Ni_{1+NPs}M@NCNT compounds than that in Ni_{1+NPs}@NCNT. The FE_{CO} values of the as-prepared Ni_{1+NPs}-M@NCNT compounds display a volcanic tendency where Ni_{1+NPs}Cu@NCNT reaches the highest value of 92.06% in an H-cell. When applied in a flow cell, the Ni_{1+NPs}Cu@NCNT exhibits an FE_{CO} of 96.92% and a current density of 171.25 mA cm^{-2} at −0.78 V (*vs.* RHE). During the galvanostatic test under 100 mA cm^{-2}, a long-lasting stability of 24 h is achieved. DFT calculation reveals that the NPs can induce electron accumulation on the Ni–N sites, thus promoting the activation of CO_2 and the stabilization of the *COOH intermediate. Meanwhile, the d-band center of Ni–N is also upshifted, offering stronger binding with reaction intermediates. In addition, NPs can also increase the Gibbs free energy change of the Volmer step, thus suppressing the competitive HER.

Conflicts of interest

The authors declare that they have no known competing financial interests or personal relationships that could have appeared to influence the work reported in this paper.

Acknowledgements

This research was supported by the National Natural Science Foundation of China (22288102, 22178019, 22208013, and 22378012) and the Fundamental Research Funds for the Central Universities (XK1802-6, XK1803-05, and XK1902). We thank the 1W1B station in Beijing Synchrotron Radiation Facility (BSRF) and BL11B station in Shanghai Synchrotron Radiation Facility (SSRF) for XAFS measurement.

References

1 S. Chu, Y. Cui and N. Liu, The path towards sustainable energy, *Nat. Mater.*, 2016, **16**(1), 16–22.
2 E. S. Sanz-Perez, C. R. Murdock, S. A. Didas and C. W. Jones, Direct Capture of CO_2 from Ambient Air, *Chem. Rev.*, 2016, **116**(19), 11840–11876.
3 X. Meng, J. Yang, C. Zhang, Y. Fu, K. Li, M. Sun, X. Wang, C. Dong, B. Ma and Y. Ding, Light-Driven CO_2 Reduction over Prussian Blue Analogues as Heterogeneous Catalysts, *ACS Catal.*, 2021, **12**(1), 89–100.
4 B. Li, M. Chen, Q. Hu, J. Zhu, X. Yang, Z. Li, C. Hu, Y. Li, P. Ni and Y. Ding, Facilely tunable dodecahedral polyoxometalate framework loaded with mono- or bimetallic sites for efficient photocatalytic CO_2 reduction, *Appl. Catal., B*, 2024, **346**, 123733.
5 D. T. Whipple and P. J. A. Kenis, Prospects of CO_2 Utilization *via* Direct Heterogeneous Electrochemical Reduction, *J. Phys. Chem. Lett.*, 2010, **1**(24), 3451–3458.
6 J. Liu, P. Li, J. Bi, S. Jia, Y. Wang, X. Kang, X. Sun, Q. Zhu and B. Han, Switching between C_{2+} Products and CH_4 in CO_2 Electrolysis by Tuning the Composition and Structure of Rare-Earth/Copper Catalysts, *J. Am. Chem. Soc.*, 2023, **145**(42), 23037–23047.
7 L. Zhang, J. Feng, L. Wu, X. Ma, X. Song, S. Jia, X. Tan, X. Jin, Q. Zhu, X. Kang, J. Ma, Q. Qian, L. Zheng, X. Sun and B. Han, Oxophilicity-Controlled CO_2 Electroreduction to C_{2+} Alcohols over Lewis Acid Metal-Doped $Cu^{\delta+}$ Catalysts, *J. Am. Chem. Soc.*, 2023, **145**(40), 21945–21954.
8 O. S. Bushuyev, P. De Luna, C. T. Dinh, L. Tao, G. Saur, J. van de Lagemaat, S. O. Kelley and E. H. Sargent, What Should We Make with CO_2 and How Can We Make It?, *Joule*, 2018, **2**(5), 825–832.
9 C. Chen, J. F. Khosrowabadi Kotyk and S. W. Sheehan, Progress toward Commercial Application of Electrochemical Carbon Dioxide Reduction, *Chem*, 2018, **4**(11), 2571–2586.
10 N. H. Han, P. Ding, L. He, Y. Li and Y. Li, Promises of Main Group Metal-Based Nanostructured Materials for Electrochemical CO_2 Reduction to Formate, *Adv. Energy Mater.*, 2020, **10**, 1902338.
11 S. Verma, B. Kim, H. R. Jhong, S. Ma and P. J. Kenis, A Gross-Margin Model for Defining Technoeconomic Benchmarks in the Electroreduction of CO_2, *ChemSusChem*, 2016, **9**(15), 1–9.
12 Q. Lu, C. Chen, Q. Di, W. Liu, X. Sun, Y. Tuo, Y. Zhou, Y. Pan, X. Feng, L. Li, D. Chen and J. Zhang, Dual Role of Pyridinic-N Doping in Carbon-Coated Ni Nanoparticles for Highly Efficient Electrochemical CO_2 Reduction to CO over a Wide Potential Range, *ACS Catal.*, 2022, **12**(2), 1364–1374.
13 B. Lu, Q. Liu and S. Chen, Electrocatalysis of Single-Atom Sites: Impacts of Atomic Coordination, *ACS Catal.*, 2020, **10**(14), 7584–7618.
14 T. N. Nguyen, M. Salehi, Q. V. Le, A. Seifitokaldani and C. T. Dinh, Fundamentals of Electrochemical CO_2 Reduction on Single-Metal-Atom Catalysts, *ACS Catal.*, 2020, **10**(17), 10068–10095.
15 Y. Wang, H. Su, Y. He, L. Li, S. Zhu, H. Shen, P. Xie, X. Fu, G. Zhou, C. Feng, D. Zhao, F. Xiao, X. Zhu, Y. Zeng, M. Shao, S. Chen, G. Wu, J. Zeng and C. Wang, Advanced Electrocatalysts with Single-Metal-Atom Active Sites, *Chem. Rev.*, 2020, **120**(21), 12217–12314.
16 B. Zhang, J. Zhang, J. Shi, D. Tan, L. Liu, F. Zhang, C. Lu, Z. Su, X. Tan, X. Cheng, B. Han, L. Zheng and J. Zhang, Manganese acting as a high-performance heterogeneous electrocatalyst in carbon dioxide reduction, *Nat. Commun.*, 2019, **10**(1), 2980.
17 J. Gu, C.-S. Hsu, L. Bai, H. M. Chen and X. Hu, Atomically dispersed Fe^{3+} sites catalyze efficient CO_2 electroreduction to CO, *Science*, 2019, **364**, 1091–1094.
18 K. Li, S. Zhang, X. Zhang, S. Liu, H. Jiang, T. Jiang, C. Shen, Y. Yu and W. Chen, Atomic Tuning of Single-Atom Fe-N-C Catalysts with Phosphorus for Robust Electrochemical CO_2 Reduction, *Nano Lett.*, 2022, **22**(4), 1557–1565.
19 X. Sun, Y. Tuo, C. Ye, C. Chen, Q. Lu, G. Li, P. Jiang, S. Chen, P. Zhu, M. Ma, J. Zhang, J. H. Bitter, D. Wang and Y. Li, Phosphorus Induced Electron Localization of Single Iron Sites for Boosted CO_2 Electroreduction Reaction, *Angew. Chem., Int. Ed.*, 2021, **60**(44), 23614–23618.
20 Y. Pan, R. Lin, Y. Chen, S. Liu, W. Zhu, X. Cao, W. Chen, K. Wu, W. C. Cheong, Y. Wang, L. Zheng, J. Luo, Y. Lin, Y. Liu, C. Liu, J. Li, Q. Lu, X. Chen, D. Wang, Q. Peng, C. Chen and Y. Li, Design of Single-Atom Co-N_5 Catalytic Site: A Robust Electrocatalyst for CO_2 Reduction with Nearly 100% CO Selectivity and Remarkable Stability, *J. Am. Chem. Soc.*, 2018, **140**(12), 4218–4221.
21 X. Wang, Z. Chen, X. Zhao, T. Yao, W. Chen, R. You, C. Zhao, G. Wu, J. Wang, W. Huang, J. Yang, X. Hong, S. Wei, Y. Wu and Y. Li, Regulation of Coordination Number over Single Co Sites: Triggering the Efficient Electroreduction of CO_2, *Angew. Chem., Int. Ed.*, 2018, **57**(7), 1944–1948.
22 L. Jiao, W. Yang, G. Wan, R. Zhang, X. Zheng, H. Zhou, S. H. Yu and H. L. Jiang, Single-Atom Electrocatalysts from Multivariate Metal-Organic Frameworks for Highly Selective Reduction of CO_2 at Low Pressures, *Angew. Chem., Int. Ed.*, 2020, **59**(46), 20589–20595.
23 X. Rong, H. J. Wang, X. L. Lu, R. Si and T. B. Lu, Controlled Synthesis of a Vacancy-Defect Single-Atom Catalyst for Boosting CO_2 Electroreduction, *Angew. Chem., Int. Ed.*, 2020, **59**(5), 1961–1965.
24 A. Guan, Z. Chen, Y. Quan, C. Peng, Z. Wang, T.-K. Sham, C. Yang, Y. Ji, L. Qian, X. Xu and G. Zheng, Boosting CO_2 Electroreduction to CH_4 *via* Tuning Neighboring Single-Copper Sites, *ACS Energy Lett.*, 2020, **5**(4), 1044–1053.

25 J. Chen, Z. Li, X. Wang, X. Sang, S. Zheng, S. Liu, B. Yang, Q. Zhang, L. Lei, L. Dai and Y. Hou, Promoting CO_2 Electroreduction Kinetics on Atomically Dispersed Monovalent Zn(I) Sites by Rationally Engineering Proton-Feeding Centers, *Angew. Chem., Int. Ed.*, 2022, **61**(7), e202111683.

26 F. Yang, P. Song, X. Liu, B. Mei, W. Xing, Z. Jiang, L. Gu and W. Xu, Highly Efficient CO_2 Electroreduction on ZnN_4-based Single-Atom Catalyst, *Angew. Chem., Int. Ed.*, 2018, **57**(38), 12303–12307.

27 X. Li, W. Bi, M. Chen, Y. Sun, H. Ju, W. Yan, J. Zhu, X. Wu, W. Chu, C. Wu and Y. Xie, Exclusive Ni-N_4 Sites Realize Near-Unity CO Selectivity for Electrochemical CO_2 Reduction, *J. Am. Chem. Soc.*, 2017, **139**(42), 14889–14892.

28 A. Pedersen, J. Barrio, A. Li, R. Jervis, D. J. L. Brett, M. M. Titirici and I. E. L. Stephens, Dual-Metal Atom Electrocatalysts: Theory, Synthesis, Characterization, and Applications, *Adv. Energy Mater.*, 2021, **12**(3), 2102715.

29 T. N. Huan, N. Ranjbar, G. Rousse, M. Sougrati, A. Zitolo, V. Mougel, F. Jaouen and M. Fontecave, Electrochemical Reduction of CO_2 Catalyzed by Fe-N-C Materials: A Structure-Selectivity Study, *ACS Catal.*, 2017, **7**(3), 1520–1525.

30 Y. Cheng, S. Zhao, B. Johannessen, J. P. Veder, M. Saunders, M. R. Rowles, M. Cheng, C. Liu, M. F. Chisholm, R. De Marco, H. M. Cheng, S. Z. Yang and S. P. Jiang, Atomically Dispersed Transition Metals on Carbon Nanotubes with Ultrahigh Loading for Selective Electrochemical Carbon Dioxide Reduction, *Adv. Mater.*, 2018, **30**(13), 1706287.

31 W. Ren, X. Tan, C. Jia, A. Krammer, Q. Sun, J. Qu, S. Smith, A. Schueler, X. Hu and C. Zhao, Electronic Regulation of Ni Single Atom by Confined Ni Nanoparticles for Energy-Efficient CO_2 Electroreduction, *Angew. Chem., Int. Ed.*, 2022, e202203335.

32 W. Liu, P. Bai, S. Wei, C. Yang and L. Xu, Gadolinium Changes the Local Electron Densities of Nickel 3d Orbitals for Efficient Electrocatalytic CO_2 Reduction, *Angew. Chem., Int. Ed.*, 2022, e202201166.

33 T. Zhang, X. Han, H. Yang, A. Han, E. Hu, Y. Li, X. Q. Yang, L. Wang, J. Liu and B. Liu, Atomically Dispersed Nickel(I) on an Alloy-Encapsulated Nitrogen-Doped Carbon Nanotube Array for High-Performance Electrochemical CO_2 Reduction Reaction, *Angew. Chem., Int. Ed.*, 2020, **59**(29), 12055–12061.

34 S. Liang, Q. Jiang, Q. Wang and Y. Liu, Revealing the Real Role of Nickel Decorated Nitrogen-Doped Carbon Catalysts for Electrochemical Reduction of CO_2 to CO, *Adv. Energy Mater.*, 2021, **11**(36), 2101477.

35 S. Bai, L. Tan, C. Ning, G. Liu, Z. Wu, T. Shen, L. Zheng and Y. F. Song, Revealing the Kinetic Balance between Proton-Feeding and Hydrogenation in CO_2 Electroreduction, *Small*, 2023, e2300581.

36 S. Li, M. Ceccato, X. Lu, S. Frank, N. Lock, A. Roldan, X.-M. Hu, T. Skrydstrup and K. Daasbjerg, Incorporation of nickel single atoms into carbon paper as self-standing electrocatalyst for CO_2 reduction, *J. Mater. Chem. A*, 2021, **9**(3), 1583–1592.

37 Q. Zhang, P. Kumar, X. Zhu, R. Daiyan, N. M. Bedford, K. H. Wu, Z. Han, T. Zhang, R. Amal and X. Lu, Electronically Modified Atomic Sites Within a Multicomponent Co/Cu Composite for Efficient Oxygen Electroreduction, *Adv. Energy Mater.*, 2021, **11**(17), 2100303.

38 L. Zhang, J. Feng, S. Liu, X. Tan, L. Wu, S. Jia, L. Xu, X. Ma, X. Song, J. Ma, X. Sun and B. Han, Atomically Dispersed Ni-Cu Catalysts for pH-Universal CO_2 Electroreduction, *Adv. Mater.*, 2023, e2209590.

39 X. Chen, X. T. Wang, J. B. Le, S. M. Li, X. Wang, Y. J. Zhang, P. Radjenovic, Y. Zhao, Y. H. Wang, X. M. Lin, J. C. Dong and J. F. Li, Revealing the role of interfacial water and key intermediates at ruthenium surfaces in the alkaline hydrogen evolution reaction, *Nat. Commun.*, 2023, **14**(1), 5289.

40 X. Liao, R. Lu, L. Xia, Q. Liu, H. Wang, K. Zhao, Z. Wang and Y. Zhao, Density Functional Theory for Electrocatalysis, *Energy Environ. Mater.*, 2021, **5**(1), 157–185.